3D-printed glass microfluidics for fluid dynamics and rheology

Noa Burshtein[1], San To Chan[1], Kazumi Toda-Peters,
Amy Q. Shen and Simon J. Haward

Abstract

Microfluidics provides a versatile platform for handling small volumes of fluids at small length scales. From a fluid dynamics perspective, microfluidics gives access to a regime of very high deformation rates $\dot{\gamma}$ at moderate to negligible Reynolds numbers Re. For viscoelastic fluid flows, the resulting high Weissenberg numbers $Wi = \tau\dot{\gamma}$, where τ is the fluid characteristic time, means the flow occurs at high elasticity number $El = Wi/Re$. Consequently, microfluidics supports a burgeoning interest in the experimental study of purely elastic flow instabilities and elastic turbulence. However, for rheological studies, typical microfluidic fabrications by soft lithography in poly (dimethyl siloxane) suffer from a number of limitations arising from the low elastic modulus and poor optical properties of the material. In this review, we summarise a few recent studies from our group in which we have experimented with microdevice fabrications using the subtractive three-dimensional (3D)-printing technique of selective laser-induced etching (SLE). SLE can be used to fabricate arbitrary 3D geometries with micron precision in fused silica: a high modulus, highly transparent material, which is robust and resistant to organic solvents. Apart from high elasticity number flows, we have found that SLE fabricated devices can sustain very high deformation rates without device failure, providing new access to little-explored inertio-elastic regimes in extremely dilute polymer solutions. Furthermore, it is possible to visualize flows from multiple planes of observation, allowing the quantitative study of 3D flow instabilities and vortex dynamics in both Newtonian and non-Newtonian fluids. SLE fabrication offers many new opportunities to those involved in fluid dynamics and rheology research at the microscale, and we highlight what we perceive as potentially fruitful ideas for future studies using this technique.

Addresses

Okinawa Institute of Science and Technology Graduate University, 1919-1 Tancha, Onna-son, Okinawa 904-0495, Japan

Corresponding author: Haward, Simon J (simon.haward@oist.jp)
[1] Equal contribution.

Introduction

Microfluidics is the study of flows in geometries with a characteristic length scale $\ell \lesssim 1000\mu m$ [1−4]. Over recent decades, microfluidics has become a central pillar in research on rheology and non-Newtonian fluid dynamics, with nearly all related international conferences now offering dedicated microfluidic sessions in the programme. For the rheologist, the basic interest of microfluidics stems from the fact that a given average flow velocity U leads to high deformation rates $\dot{\gamma} \sim U/\ell$. For viscoelastic fluids such as polymer or micellar solutions, with a dissolved microstructure that relaxes on a timescale τ, high Weissenberg numbers $Wi = \tau\dot{\gamma}$ can, thus, be attained, enhancing the importance of elastic effects in the flow [5]. On the other hand, the strength of inertial effects in the flow, described by the Reynolds number $Re = \rho U \ell/\eta$ (where ρ is the density and η is the viscosity of the fluid), can be kept moderate or negligible. Through microfluidics, the rheologist can, thus, study the effects of fluid elasticity without being concerned by complications arising from inertia. These flows are typically described by high elasticity numbers $El = Wi/Re \simeq \tau\eta/\rho\ell^2$. The enhancement of elastic effects at the microscale leads to applications in rheometry with even low viscosity fluids with short relaxation times. Such fluids would have low El at the macroscale and hence be difficult to characterize by standard techniques because of inertial complications. Microfluidic devices have been used to show how polymers and micelles deform in response to flows [6−11] and are central to the study of purely elastic instabilities and elastic turbulence that can arise even in inertialess flows due to flow deformation feedback [12−27].

While the potential benefits of small size scales in non-Newtonian flow experiments have always been clear and were exploited in a few early cases dating back to the 1980s (e.g. Refs. [28,29]), the use of microfluidic geometries in rheology research became more widespread after the development of soft lithography techniques for fabrication of devices [1]. Fabrication in poly (dimethyl siloxane) (PDMS) became the norm and remains by far the most common method for producing microfluidic devices in laboratory settings today. PDMS fabrication typically starts by the generation of a master (or mould) by patterning a photoresistive material on a silicon wafer using photolithography. Liquid resin (typically a 10:1 mixture of base PDMS and a curing agent) is then poured over the mould and cured in an oven. Once cured, the PDMS is rubbery and elastic. Hence, it can simply be peeled away from the mould, which can be reused to fabricate more devices. The cured PDMS is bonded to a glass slide or cover slip to enclose the channels. This is performed either by coating the slide with another thin layer of PDMS to act as an adhesive or by using oxygen plasma to activate the two surfaces to be bonded. Either before or after bonding, holes are punched through the PDMS to connect the tubing to the inlets and outlets of the microchannel.

Fabrication in PDMS is relatively cheap, easy and rapid, and much progress has been made in understanding microscale viscoelastic flows using PDMS devices. However, such soft lithography does have disadvantages, particularly for rheological studies. The softness of PDMS means that channels deform under the pressure of an imposed flow, thus causing variability and uncertainty in channel dimensions. The deformation of the cross-linked polymeric material also leads to birefringence, which is problematic for accurate rheo-optical measurements designed to measure fluid stresses [30]. The material softness also results in sagging or collapse of channels of high (or low) aspect ratio, restricting this important parameter to a narrow usable range. The PDMS has rather poor optical properties, so viewing access into the channel is practically restricted to one side, i.e. through the glass cover slide. The bonding of the PDMS to a glass slide is often too weak to withstand the pressure resulting from flows at high rates, leading to delamination and leakage of fluid. Device failure is also frequent at the inlet and/or outlet connection points. The PDMS material is not compatible with organic solvents, which cause it to swell; therefore, studies with polymeric fluids are restricted to just a few types of water-soluble polymers. It is also difficult to effectively clean a PDMS device subsequent to an experiment. PDMS devices are essentially disposable; frequent device failures and inability to clean devices effectively limits their useful lifetime. A comprehensive series of rheological experiments may, thus, require fabrication of a number of such devices, no two of which will be identical (albeit fabricated from the same mould). For obvious reasons, this is not an ideal scenario. Finally, fabrications in PDMS by soft lithography are restricted to planar (two-dimensional [2D]) geometries (or at best to 2.5D, by a complicated multilayer process), although we note recent developments in three-dimensional (3D) PDMS fabrications by means of soluble moulds that can be 3D-printed or formed from sucrose [31,32].

Some of the disadvantages of PDMS-based devices can be avoided by using other fabrication techniques such as laser cutting [33], wire electrical discharge machining (wire-EDM) [34], micromilling [35], reactive ion etching [36], or chemical etching in silicon or glass [36]. However, none of these approaches provide a complete solution because none is amenable to 3D fabrication; most are restricted to rather low aspect ratio devices, and most have optical access limited to only one plane.

A potentially more holistic solution to the problems encountered in soft lithography is offered by selective laser-induced etching (SLE) [37]. SLE is a relatively new subtractive 3D printing technique enabling microfabrication in transparent substrates, typically fused silica glass (SiO$_2$) [37]. The technique permits the fabrication of truly 3D structures in a high modulus (≈ 75 GPa), highly transparent (optical transmission $> 90\%$ over the whole of the visible range) material with a resolution $\sim O(1 \ \mu m)$.

SLE is a two-step process involving the laser modification and subsequent chemical etching of the substrate. A femtosecond laser is used to irradiate a selected volume of material, thereby increasing the chemical etch rate of specific regions within the glass substrate by up to 1000 times compared with the un-irradiated material. To produce the SLE structures in our laboratory, we use the commercially available LightFab 3D printer (LightFab GmbH), which uses a 4 W, $\lambda = 1030$ nm, femtosecond-pulsed laser, with a 2.6 μm (x, y), 6 μm (z) spot size [38]. As with most 3D printing techniques, the SLE process begins with the creation of a 3D computer-aided design model (Figure 1a). The model is designed to represent the portion of the substrate that will be removed during fabrication. The 3D model is sliced to create the programmed laser paths that the LightFab scanner will use to modify the fused silica volume during the printing process (Fig. 1b). The sliced model becomes a collection of stacked xy-planar profiles separated into $\approx$ 10 μm layers; this slicing scheme alone would allow for 2D or even 2.5D vertical 'cuts' through the glass (sufficient for vertical holes through z), but to achieve a truly 3D structure, additional programmed laser paths are needed. To create a horizontal 'cut', such as on the top and bottom of an internal cavity, those slices need to be filled with an array of parallel paths with $\approx 10 \ \mu m$ spacing. Great care should be taken in optimising the slicing and filling of the volume: if the programmed

Figure 1
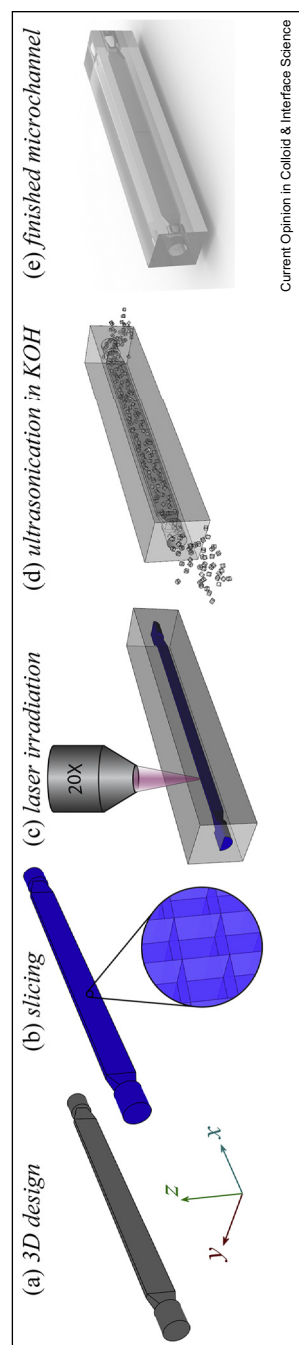
Fabrication by selective laser-induced etching: (a) The inner volume of a desired microfluidic channel is created using 3D CAD software. **(b)** The 3D model is then sliced and filled to create a *z*-stack of lines used to define individual laser paths. **(c)** A femtosecond laser irradiates a polished fused silica substrate following the specified slices. **(d)** The laser-irradiated material is preferentially etched by KOH (assisted by ultrasonication at 85°). **(e)** The finished monolithic glass microfluidic device. 3D, three-dimensional; CAD, computer-aided design. The finished microfluidic channel is removed. **(e)** The inner volume of the microfluidic channel is removed.

(a) *3D design* (b) *slicing* (c) *laser irradiation* (d) *ultrasonication in KOH* (e) *finished microchannel*

Current Opinion in Colloid & Interface Science

laser paths are too dense, overlap frequently or form too many sharp corners, it is easy to induce cracking of the substrate during the subsequent laser modification or wet etching steps. Creating the laser paths for an SLE structure is a compromise between achieving the most accurate representation of a desired 3D model and fabricating a structure without failure. A densely sliced and filled structure will more accurately reproduce the desired geometry and etch faster but presents a higher risk of failure. A less densely sliced and filled structure has a lower chance of developing cracks but will etch more slowly and may result in reduced fidelity to the specified design.

Owing to the compromise between densely and minimally filled SLE structures, an appropriate slicing and filling scheme needs to be chosen. Often an internal cubing scheme is chosen (Figure 1b) to break up the internal volume of material into smaller volumes that can be easily removed via the narrow inlet and/or outlet regions during the subsequent ultrasonic wet etching step. Once the programmed laser path file and a polished fused silica substrate are loaded into the LightFab, laser modification can begin (Figure 1c). The LightFab uses the combination of a galvanometer scanner to laser modify a whole *xy*-tile ($700 \times 700 \ \mu$m with a $20\times$ objective lens). The objective lens is mounted on a $200 \ \mu$m high-speed piezo *z*-stage to stack the tiles vertically and a motorized *xyz*-stage to stitch the $700 \times 700 \times 200$ iμm tile stacks together. The stitching of these tiled regions allows for the precise laser modification of the entire structure in a fraction of the time when compared with direct line by line laser modification. The laser-modified fused silica substrate is then placed in an 85°C KOH ultrasonic bath to perform the chemical etching (Figure 1d). The laser-modified regions of the fused silica etch at a rate of between 50 and $100 \ \mu$m hr^{-1} (compared with $\approx 0.1 \ \mu$m hr^{-1} for the unmodified regions), allowing the removal of specified regions within the material. After etching is complete, the device is rinsed with deionized water and is ready for use (Figure 1e).

In this review article, we highlight recent and ongoing work from our laboratory, in which we have used SLE to fabricate novel flow geometries. Even though we are new users of this technology and our designs, so far, remain relatively simple, SLE has enabled experimental measurements that would be extremely difficult (even impossible) to carry out in channels made by other currently available methods. We believe there is great potential for SLE to make a major impact in the microfluidics, fluid dynamics, and non-Newtonian flow communities by opening the door to imaginitive new experimental geometries and the possibility to visualize 3D microscopic flows. We conclude our review with a short perspective outlining our vision for the future potential of SLE within these fields.

Flow around low blockage ratio microfluidic cylinders

The classical problem of the flow around a cylinder is considered a benchmark in non-Newtonian fluid dynamics, being relevant to understanding a wide range of practical flows, including particle sedimentation and flow through porous media. Study of viscoelastic flows around cylinders has a rich history at the macroscale and has recently been attracting significant efforts at the microscale. However, attempts to fabricate microfluidic cylinder devices from PDMS are restricted in two respects: (1) to avoid a large deformation of the cylinder under the flow, its radius r is made large compared with its height H and (2) to accommodate the cylinder, the channel width W must also be large compared with the height H. The result is a channel with a low aspect ratio (typically $\alpha = H/W \ll 1$) that is largely blocked by the cylinder (blockage ratio $\beta = 2r/W \geq 0.5$) [25,39]. In viscoelastic flows, the resulting narrow gaps between the cylinder and the channel side walls dominate the rheological response, driving recirculations upstream of the cylinder and masking other aspects of the flow field such as the important regions of the elongational flow near the leading and trailing stagnation points.

We exploited various features of SLE fabrication in fused silica (high resolution, high material modulus and good optical properties) to produce novel microfluidic cylinder geometries with a high aspect ratio ($\alpha = 5$) and a low blockage ratio ($\beta = 0.1$), see Figure 2a–d [40]. The channel width and height and the cylinder radius are $W = 400 \ \mu m$, $H = 2000 \ \mu m$, and $r = 20 \ \mu m$, respectively. A dilute (700-wppm) viscoelastic solution of a nearly monodisperse 6.9 MDa poly (styrene) in an organic solvent was tested in the device (possible because of the inert glass construction). The solution viscosity was $\eta = 71$ mPa s, and the relaxation time was $\tau = 13$ ms. The small characteristic length r gave access to high Wi for negligible Re. As is evident from Figure 2b–d, the cylinder can be viewed from both the side and the end-on perspectives, which allows the flow field to be characterised in detail by micro-particle image velocimetry (μ-PIV) [41]. Although the cylinder is very slender ($H/2r = 50$), the high elastic modulus means it can be considered effectively rigid, with deformation on the order of the surface roughness (i.e. $\sim 1 \ \mu m$) even at the highest flow rates examined [40].

In stark contrast to typical PDMS microscale cylinder geometries with high values of β, our SLE fabricated device with $\beta = 0.1$ clearly reveals the strongly deforming nature of the leading and trailing stagnation points (Figure 2e–h). While at low $Wi \lesssim 1$, the flow appears Newtonian like (Figure 2e), at progressively higher Wi, the flow field around the cylinder becomes significantly modified, particularly in an increasingly extended downstream wake (Figure 2f and g). The relatively large channel height (hence, approximately 2D flow profile), together with the high transparency and low birefringence of the fused silica device, allow meaningful flow-induced birefringence measurements to be made, revealing the local regions of high polymer orientation and tensile stress in the flowing fluid (Figure 2h) [30]. This allows the flow modification around the cylinder to be understood in terms of localised increases in the extensional viscosity of the fluid due to macromolecular orientation in the strong streamwise velocity gradients near the stagnation points. We have also looked at the flow around a second cylinder located within the flow-modified wake region, revealing insights into the nature of the interactions between bubbles, drops, and particles in viscoelastic fluid flows [40,42].

Flows through intersecting geometries
Vortex formation in cross-slot flow

The cross-slot flow geometry consists of two bisecting rectangular channels of width w and depth d (aspect ratio $\alpha = d/w$). Under creeping flow conditions, injecting fluid into two opposing inlets and withdrawing fluid from the remaining two outlets (all at equal volumetric rates) results in the symmetric division of streamlines around a central hyperbolic point located at $x = y = 0$ and the generation of a planar elongational flow field with a stretching component along the outlet direction (x), see Figure 3a. This canonical flow configuration is widely used in the microfluidics and rheology communities for, for example, hydrodynamic trapping, studying macromolecular dynamics and performing extensional rheometry [43]. However, the cross-slot flow can become unstable at surprisingly low values of a critical Reynolds number ($Re_c \approx 40$ for $\alpha = 1$ and taking w as the characteristic length). For $Re > Re_c$, a symmetry-breaking bifurcation leads to the formation of a steady streamwise stretched vortex (reminiscent of a Burgers vortex [44,45]) that propagates downstream along the outlet channels [46].

Traditional fabrication processes yield cross-slots with good optical access to the stagnation point region in xy planes only, so visualization of the spiral vortex structure in the orthogonal yz plane was only possible by imaging of dye advection patterns using scanning confocal microscopy, see Figure 3a [46,47]. Such imaging can provide a good qualitative impression of the resulting structures in steady flows and can be used to quantify the mixing efficiency. However, dynamic studies are not possible, and performing detailed quasistatic sweeps through a range of Re is extremely difficult due to the long scanning times. Furthermore, imaging of dye advection provides no quantitative information of the flow field, which is both highly desirable and necessary to allow a proper comparison with numerical simulations [46,48,49].

Figure 2
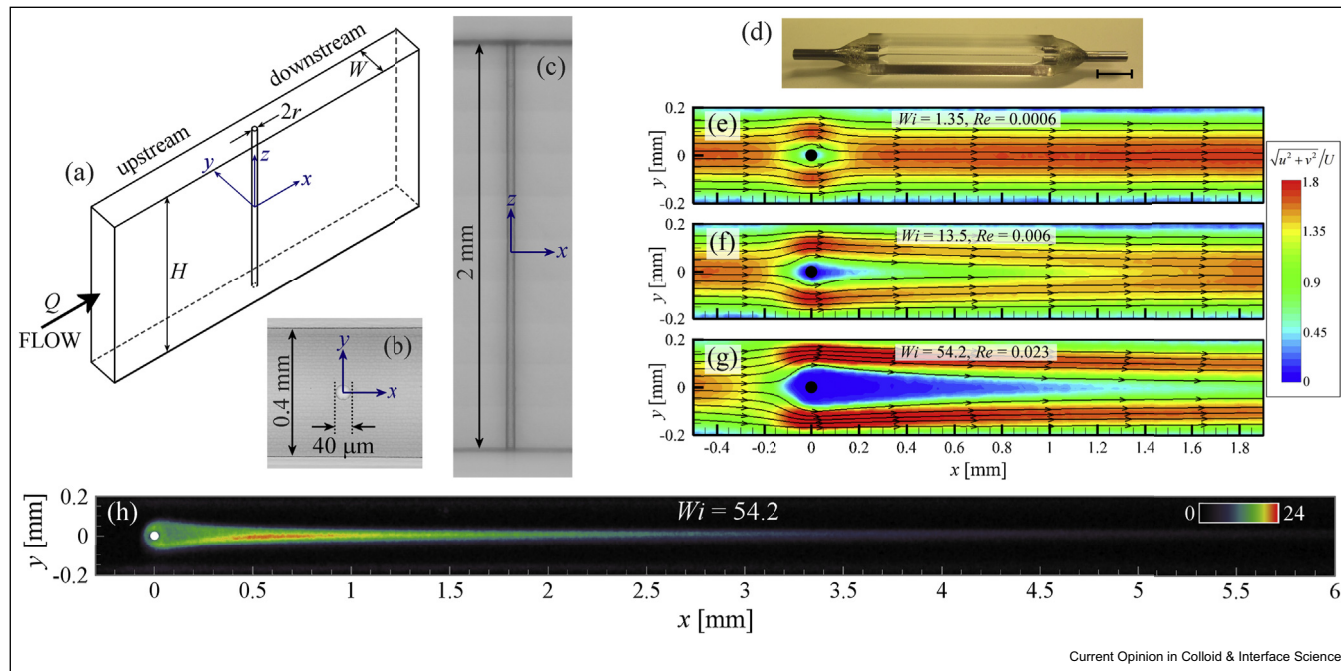
Flow around microfluidic cylinders: **(a)** Schematic representation of the flow configuration and micrographs of the cylinder taken from **(b)** top and **(c)** side views; **(d)** shows the complete device after assembly: scale bar represents 5 mm. **(e–g)** Flow velocity fields around the cylinder as the Weissenberg number is progressively increased. **(h)** Flow-induced birefringence in the cylinder wake measured at high Weissenberg number, $Wi = 54.2$. Parts (a) and (e−h) reproduced from Ref. [40], with permission from Elsevier.

Figure 3
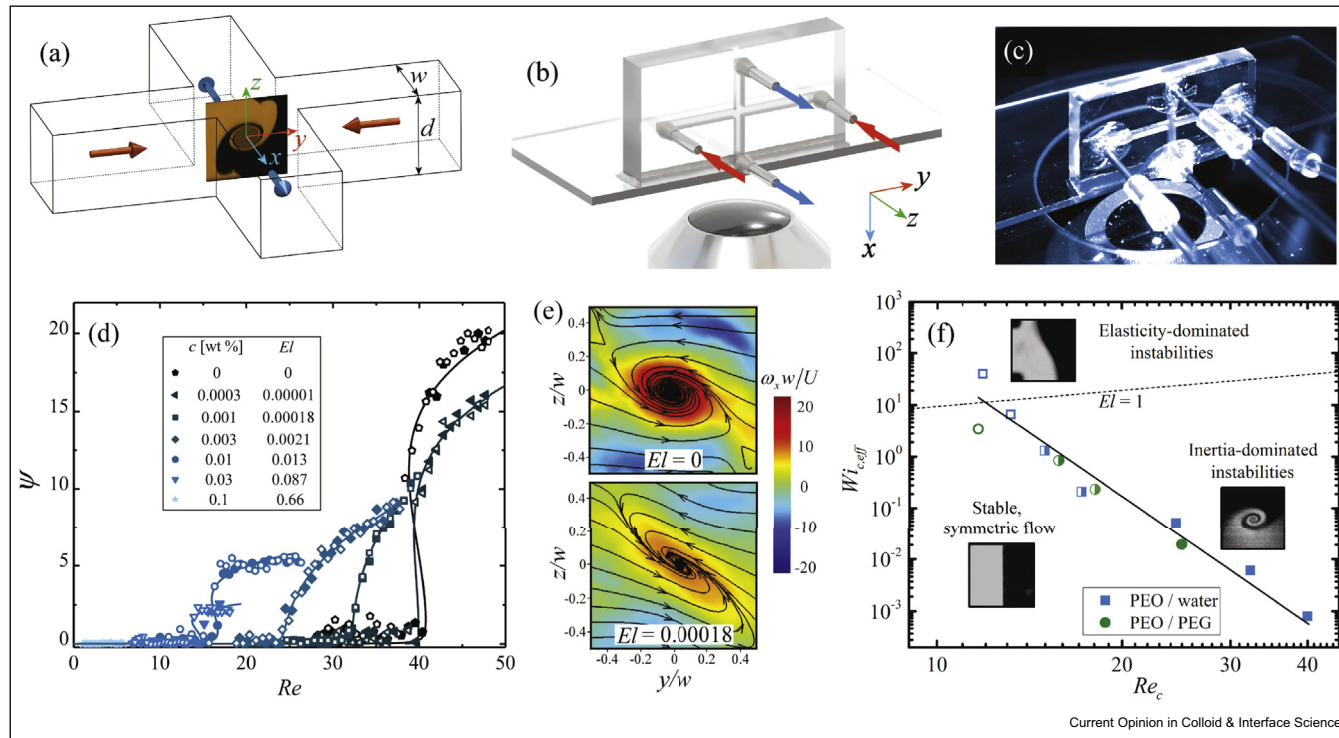
Vortex formation in a cross-slot geometry: (a) Schematic diagram of a cross-slot device where w is the width and d is the depth of the channel. Inflow and outflow are along the y and x directions indicated by red and blue arrows, respectively. Beyond a critical Reynolds number, a streamwise vortex forms at the centre of the geometry and propagates downstream. **(b)** Schematic representation of vertical mounting of a microfluidic cross-slot device, enabling a direct observation of an outlet channel cross-section. **(c)** Photograph of the actual experimental set-up, with a cross-slot ($w = d = 420 \ \mu m, \alpha = 1$) mounted on an inverted microscope. **(d)** The order parameter ψ as a function of Re for PEO dissolved in water. Closed and open symbols indicate data obtained with quasistatic increases and decreases in Re, respectively. The solid lines are fits using the Landau model. **(e)** Flood-filled μ-PIV images of the dimensionless vorticity over the $x = 0$ plane for water (top) and a $c = 0.001$ wt% PEO solution at the same $\varepsilon = 0.15$. **(f)** Stability diagram in Wi_{eff}, Re dimensionless space. Inserts are snapshots of fluorescent dye patterns indicating the nature of the flow within the three broad regimes. PEO, poly(ethylene oxide); μ-PIV, micro-particle image velocimetry. Adapted from Ref. [48].

In a recent article, we have shown how SLE can be used to construct a cross-slot geometry with good optical access to both the xy and yz planes, see Figure 3b and c [48]. This configuration allows quantitative full-field, time-resolved μ-PIV and computation of the axial component of the vorticity ω_x to be performed in the cross-section of an outlet channel; using a long working distance lens, measurements are even possible at the $x = 0$ plane (Figure 3d and e). Performing quasistatic experiments with small increments in Re and also dynamic flow studies are rendered relatively trivial using this modified setup. We applied this novel microfluidic device to measure the effects of dilute polymeric additives (at drag-reducing concentrations [50,51]) on the formation and development of the vortex over a wide range of the Reynolds number.

Aqueous solutions of a commercial high−molecular-weight poly (ethylene oxide) (PEO, M_w = 4 MDa) were used to study the effect of polymer additives on vortex formation in the cross-slot device. The polymer concentration was varied in the range of $0 \leq c \leq 0.1$ wt%, thus modifying both the zero-shear viscosity η_0 and the relaxation time τ of the fluid. For some of the fluids, we also enhanced the solvent viscosity η_s by the addition of a low−molecular-weight poly (ethylene glycol). The resulting variation in rheological properties provided fluids with a wide range of elasticity numbers $0 \leq El \leq$ 10.4. Here, we define $El = Wi_{eff}/Re$, where the 'effective Weissenberg number' $Wi_{eff} = Wi(1 - \beta)$, and $\beta = \eta_s/\eta_0$ is the solvent-to-total viscosity ratio. This definition accounts for the stress carried by the solvent, which becomes an important consideration at low polymer concentrations.

Figure 3d shows the nondimensionalised centre−point axial vorticity $\psi = (w/U)\omega_x|_{x=y=z=0}$ measured as a function of Re for a series of PEO solutions in pure water. We observe that as the polymer concentration and hence El are progressively increased, the vorticity begins to grow when Re exceeds a progressively lower critical value. Furthermore, the growth of the vorticity is significantly suppressed by the polymer additive, even at the lowest concentrations tested. Indeed, for the sample with $c = 0.1$ wt% PEO ($El = 0.66$), no increase of the vorticity is observed before a contrasting instability is encountered consistent with the widely reported purely elastic mode [15,54]. The data in Figure 3d are well described using a sixth-order Landau-type model $\varepsilon = (Re - Re_c)/Re_c = k\psi^4 + g\psi^2 - h\psi^{-1}$. Figure 3e shows vorticity fields for a Newtonian fluid ($El = 0$) and a weakly elastic PEO solution ($El = 0.00018$) at the same value of $\varepsilon = 0.15$, graphically demonstrating the vorticity suppression by the polymer additive.

Figure 3f summarises the experimental findings in the form of a phase diagram in Wi_{eff} *versus* Re state space.

Remarkably, the critical conditions for flow instability in all our tested polymeric fluid samples collapse onto a single line. We identify three regions in the diagram; left of the stability boundary, that is, for low Re and low Wi_{eff}, the flow remains stable and symmetric. For weakly elastic fluids (low Wi_{eff} but relatively high Re), steady streamwise vortices are generated to the right of the boundary. Following the boundary back to lower Re and higher Wi_{eff}, the purely elastic instability mode arises for $El \gtrsim 1$. In between is a transitional region characterized by formation of weak and spatiotemporally fluctuating vortical structures [48].

Vortex breakdown in dividing T-channel flow

Researchers have also explored how low-density particles interact with the 3D vortical flow field in the outlets of a dividing T-channel, where one inflow splits into two opposite outflows, see Figure 4. Vigolo et al. [55] first reported the unexpected trapping of air bubbles in the two outlet channels, when the inlet Reynolds number Re_{in} is above a critical value $Re_e \approx 350$. By numerical simulation, they also derived a critical density ratio $\rho_p/\rho \approx 0.7$ (where ρ_p and ρ are the densities of the particles and the fluid, respectively), below which particle trapping occurs. Chen et al. [52] then demonstrated numerically that four flow recirculation zones exist within the two outlets on a critical $Re_s \approx 320$. By the rather good agreement between Re_e and Re_s, they inferred that the bubble trapping was caused by the recirculation zones. Subsequently, Ault et al. [56] systematically studied how the recirculation zones are affected by the junction angle. By analyzing the flow fields from their simulation, they argued that such flow recirculation was caused by the bubble-type vortex breakdown, the sudden development of internal stagnation points in a swirling flow when Re is increased. Recently, Oettinger et al. [53] showed that the interaction between the suspended particles and the vortex breakdown regions was more complicated than previously thought. Their study demonstrated the existence of an 'invisible anchor', whose size is much larger than the recirculation zones, inside which the particles will flow towards the recirculation zones and become trapped.

The studies summarised previously paved the way for understanding how low-density particles interact with a dividing T-channel flow at moderate Re. We took a step further using T-channels fabricated by SLE [57]. As shown in Figure 4a−d, a similar geometrical reconfiguration to that used with the cross-slot enabled us to visualise the flow in the T-channel from multiple perspectives and hence to characterise the flow in the outlet channels in detail experimentally. The channels had dimensions $H = L = 420 \pm 10 \ \mu m$. Reynolds numbers Re_{in}, Re_1 and Re_2 were imposed at the inlet and the two respective outlets, where $Re_1 + Re_2 = Re_{in}$ and L is the characteristic length. By seeding fluorescent

Figure 4
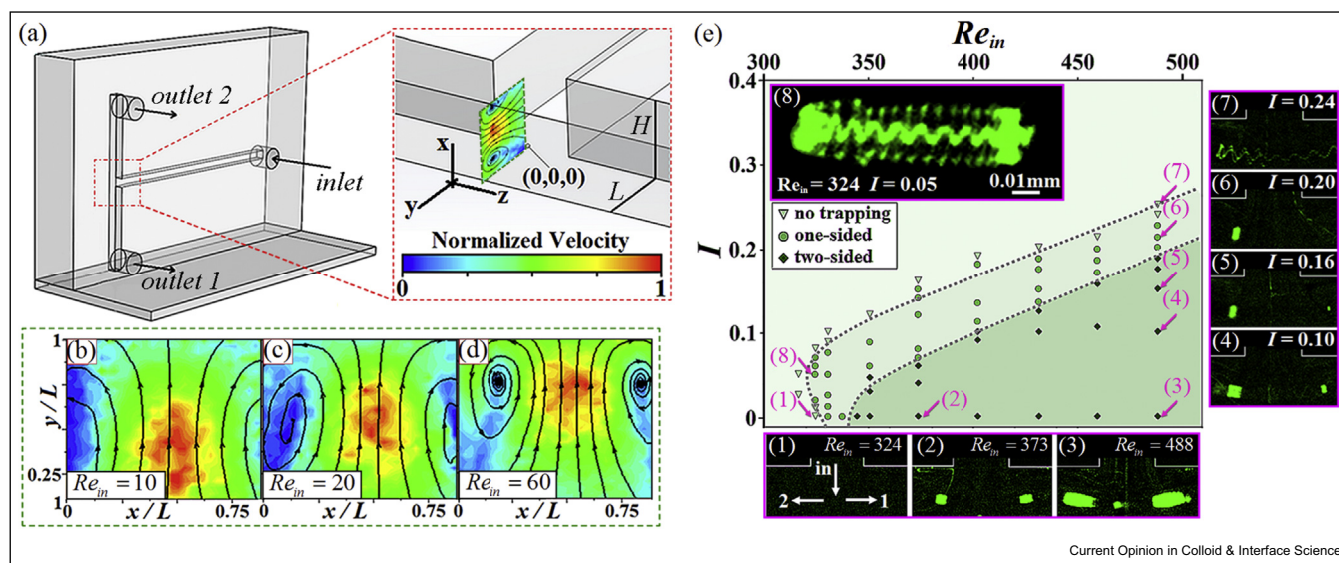
Particle trapping in a dividing T-junction flow: **(a)** Schematic diagram of the experimental setup. The inlet Reynolds number is Re_{in}, while the respective outlet Reynolds numbers are Re_1 and Re_2. **(b)−(d)** μ-PIV on the $x - y$ plane showing vortex formation in outlet 1 as Re_{in} is increased. **(e)** Phase diagram of particle trapping in a T-junction flow. Here, an imbalance factor is defined as $I = (Re_1 - Re_2)/Re_{in}$. Flow visualization images **(1)−(7)** show how the shape of the particle-trapping regions changes with Re_{in} and I. Image **(8)** shows a single particle trajectory, which resembles the numerically predicted vortex breakdown. μ-PIV, micro-particle image velocimetry. Adapted from Ref. [57].

polystyrene particles into 0.2 M sodium metatungstate solution ($\rho_p/\rho \approx 0.7$), we were able to visualise clearly the complete particle trajectory inside the flow recirculation zones, see Figure 4e, providing the first unambiguous experimental confirmation of the flow recirculation bubbles reported by simulations [57]. The highly precise and nondeformable channel dimensions also permitted a meaningful study of the effect of outflow imbalances, by setting $Re_1 \neq Re_2$. An imbalance factor was defined as $I = (Re_1 - Re_2)/Re_{in}$. The effect of imposing an outflow imbalance is to generate a pressure difference across the outlets and hence to vary the rate of vorticity decay in each outlet for a fixed level of swirl (which is set by Re_{in}). As a result, by manipulating Re_{in} and I, it was possible to trap particles in either one or both of the outlets and to vary the relative sizes of the trapping regions. As shown in the phase diagram and associated visualisations in Figure 4e, outflow imbalances of only a few percent can significantly affect the structures of the trapping regions. Apart from having potential applications for hydrodynamic manipulation of bubbles, cells and particles in microfluidics, it is important to be aware of the effects of such small imbalances, which could easily occur inadvertantly because of inaccurate device fabrication or inadequate flow control.

Spanwise vorticity in wavy channel flow

Flows over wavy surfaces (shown schematically for the channel flow in Figure 5a) induce spanwise vorticity perturbations in the fluid [58−61]. For laminar Newtonian flows, the perturbation vorticity is maximal at the wavy surface and decays with distance into the channel over a penetration depth $\mathscr{P}$. Predictions of linear theory (in 2D) reveal three regimes of flow, depending on two dimensionless parameters: (1) the normalised channel depth $\alpha = kd$, where $k = 2\pi/\lambda$, and λ is the undulation wavelength and (2) the normalised viscous length $\theta = (\eta k^2/\rho\dot{\gamma}_w)^{1/3} \simeq (\alpha^2/Re)^{1/3}$, where $\dot{\gamma}_w$ is the wall shear rate. A 'shallow viscous' regime occurs for $\alpha \lesssim 1$ and $\theta > \alpha$, in which the perturbation completely fills the flow domain ($\mathscr{P} = \alpha$). A 'deep viscous' regime is found for $\alpha \gtrsim 1$ and $\theta > 1$: in this case, the perturbation decays within the flow domain over approximately one wavelength ($\mathscr{P} \approx 1$). Finally, an 'inviscid' regime is found for $\alpha > \theta$ and $\theta < 1$: here, the perturbation decays within the flow domain within one viscous length from the surface ($\mathscr{P} \sim \theta$) [58].

Using SLE, we achieved fabrication of microchannels with sufficiently high aspect ratio and with accurately defined sinusoidal wavy surfaces with sufficiently small amplitude A to match the conditions prescribed by the 2D linear theory [60]. Five channels were made with different surface wavelengths spanning the shallow ($\alpha < 1$) and deep ($\alpha > 1$) regimes. Examples of a shallow channel at $5\times$ magnification and a deep channel at $10\times$ magnifications are shown in Figure 5b and c, respectively. Spatially resolved μ-PIV was used to measure wall-normal velocity perturbations v' for Newtonian flow in the five devices over a wide range of θ, from which the three predicted flow regimes were clearly apparent for the first time experimentally (Figure 5d).

Recent linear theory for viscoelastic wavy flows have made intriguing predictions of the amplification of perturbations in a 'critical layer', a dimensionless distance $\Sigma \simeq \alpha\sqrt{2El}$ away from the surface undulation [59,61]. A counter-intuitive implication of the prediction is that the critical layer is only found within the flow domain for relatively low values of $El \lesssim 0.5$: for $El > 0.5$, $\Sigma > \alpha$, so the critical layer has no effect on the flow! Using a deep wavy channel ($\alpha = 3.2\pi \approx 10$) and two contrasting PEO solutions with $El \approx 0.01$ (termed 'weak') and $El \approx 10$ (termed 'strong'), we tested this prediction experimentally [61]. Figure 5e shows normalised wall-normal velocity perturbation fields for Newtonian flow (top) and for the 'weak' polymeric solution (bottom) as the viscous length is progressively decreased from left to right. For Newtonian flow, the perturbations decay more closely to the wavy wall as θ is decreased below unity, as expected when transitioning between the deep viscous and the inviscid regimes. At high θ (low Wi), perturbations observed in the 'weak' polymer solution appear Newtonian like. However, as θ is decreased and Wi increases, the perturbations penetrate more deeply into the channel (opposite from Newtonian-like behaviour) and are also clearly tilted forward by the shear. Figure 5f shows the penetration depth of the perturbations measured for Newtonian fluid and also the 'weak' and 'strong' polymer solutions. Consistent with the predictions of the linear theory [59], for the 'strong' fluid, we were unable to measure any significant deviation from Newtonian behaviour. However, the 'weak' fluid displays a sudden and dramatic departure from Newtonian-like behaviour as θ is decreased below a critical value $\theta_c \approx 1$. In the insert in Figure 5f, we plot a quantity $\mathscr{P}' = \mathscr{P}_{pol} - \mathscr{P}_{Newt}$ as a function of Wi, where $\mathscr{P}_{Newt}$ and $\mathscr{P}_{pol}$ are the penetration depth of the Newtonian fluid and the weak polymer solution, respectively. We observe that the non-Newtonian increase in $\mathscr{P}$ occurs beyond a critical value of the Weissenberg number $Wi_c \approx 15$ and tends towards a plateau value as Wi becomes high. The plateau value of $\mathscr{P}' \approx 3$ indicates the location of the critical layer in the asymptotic limit of high Wi and low θ.

Very recently, using all five of our wavy channels and a range of polymer solutions with elasticity spanning $0.001 \leq El \leq 43.6$, we have experimentally constructed the full phase diagram for viscoelastic wavy channel flow, providing a full confirmation of the prior theory [59,62].

Figure 5
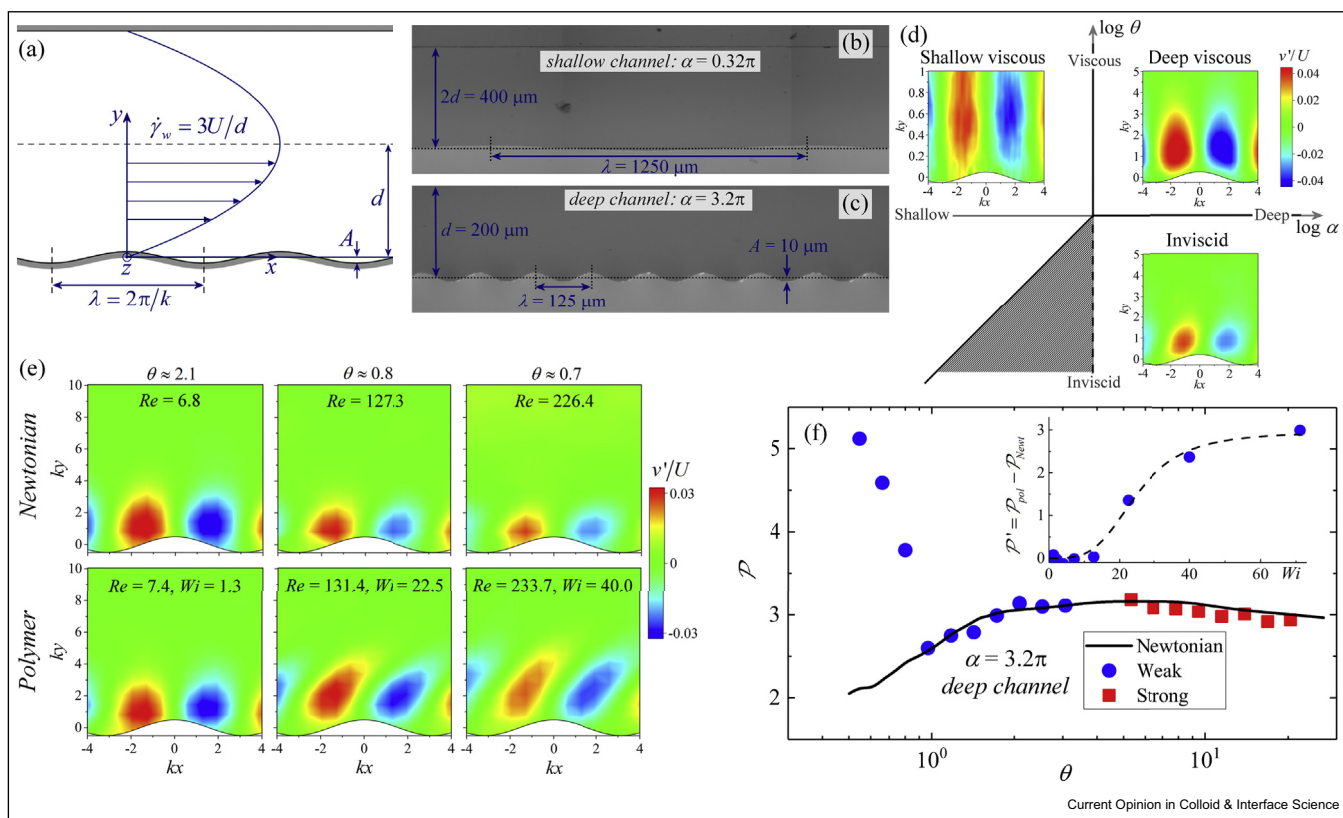
Poiseuille flow through wavy microchannels: **(a)** Schematic representation of the flow configuration and micrographs of **(b)** a shallow and **(c)** a deep wavy-walled channel fabricated by SLE. Both devices have a channel half-depth $d = 0.2$ mm, width in the spanwise (z) direction of $w = 2$ mm (aspect ratio $\alpha = w/2d = 5$), and wave amplitude $A = 10$ μm. **(d)** Experimental phase diagram for Newtonian wavy channel flow, showing v' perturbation velocity fields measured in each of the three theoretically predicted flow regimes. **(e)** v' perturbation velocity fields measured in a deep wavy channel as θ is decreased: Top: Newtonian fluid, Bottom: weakly elastic polymer solution. **(f)** Penetration depth of v' perturbations as a function of θ for a strongly elastic and a weakly elastic fluid in a deep wavy channel, compared with the Newtonian response. Insert shows how the penetration depth of the weakly elastic polymer solution increases over the Newtonian value beyond a critical Weissenberg number $Wi_c \approx 15$ and apparently approaches a plateau value as Wi becomes higher, indicating the asymptotic location of the critical layer (dashed line is guide to the eye). SLE, selective laser-induced etching. Parts (a), (e) and (f) adapted from Ref. [61].

Our experiments verify the existence of critical layers and shows that they have measureable effects on real viscoelastic flows. The consequences are potentially profound and may lend insights into the mechanisms underlying the vorticity dynamics in a range of inertioelastic flows with streamline undulation, such as elastoinertial turbulence [61,63].

Summary and outlook

In recent works, we have been examining the potential of SLE for microfluidic device fabrication with specific applications in fluid dynamical and rheological problems. Fabrication in rigid, highly transparent and chemically inert material by this high-precision subtractive 3D printing technique offers significant

Figure 6

Current Opinion in Colloid & Interface Science
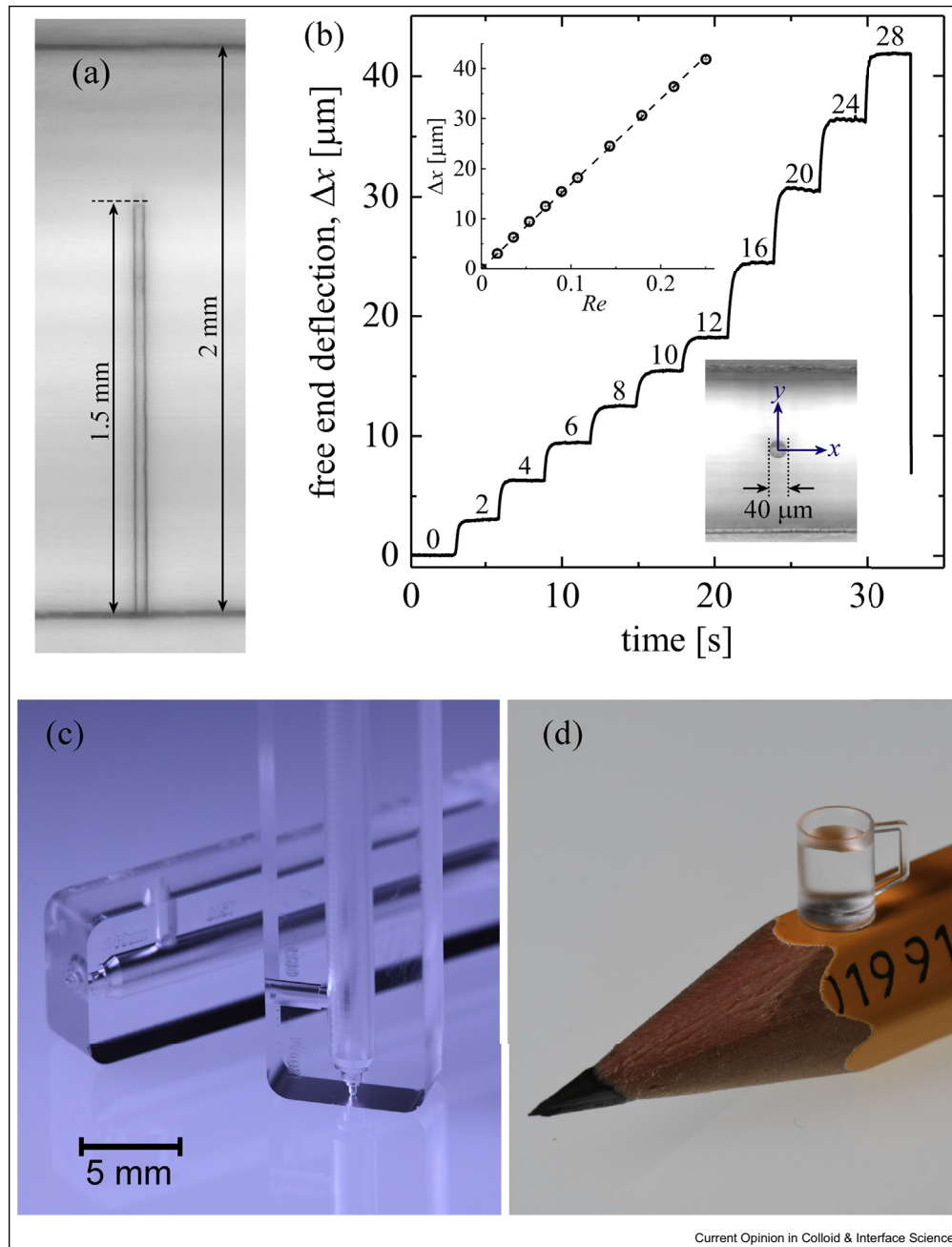
Ongoing works featuring selective laser-induced etching fabrication: (a) Side view of a free-standing post of radius $r = 20\ \mu$m contained within a microchannel, fabricated from a single piece of glass using SLE. **(b)** Deflection of the free end of the post as a function of time as the flow rate is incremented at 3-s intervals; the flow rate in mL min^{-1} is indicated by the number above each step. The top left insert shows proportionality between the deflection and the imposed Reynolds number. The bottom right insert shows a photograph of the free end of the post. **(c)** Axisymmetric SLE-fabricated geometries designed to model spray nozzles, with integrated pressure tappings entering the channels orthogonally. **(d)** 'Microfluidic' beer mug containing 20 μL of fluid and balanced on a regular pencil to indicate the scale. SLE, selective laser-induced etching.

advantages over microfabrication by other current methods and presents new opportunities for examining microscale flows in interesting and novel ways. The example studies that we have summarised in this review use relatively simple planar geometries that largely present new perspectives on well-known fluid mechanical problems (i.e., flow around cylinders and through junctions) by extending the geometrical parameter range into new regimes and/or by permitting optical access, hence measurements, to be made in previously inaccessible planes of view. Although our work is already providing significant new insights into a range of topical problems, we feel we are scratching the surface of what is possible using SLE.

Some future directions that we are currently pursuing include the fabrication of structures that can deform in response to the flow field, for example, slender posts pinned at only one end (see Figure 6a and b) or thin sheets of material fixed at one edge. This will enable the study of viscoelastic fluid–structure interactions [64,65] at the high elasticity numbers associated with the microscale, potentially lending insights into biological motions of, for example, cilia and flagella in viscoelastic media such as mucus and semen. One particular challenge that we would like to address is the integration of pressure sensors into the SLE-fabricated channels. Pressure measurement is an essential component for performing rheometry in channels at a controlled shear rate and is a highly desirable metric in all flow studies. At present, we can easily create simple pressure tappings in the channel walls that can be connected by tubes to external transducers (see e.g. Figure 6c), but sensors flush with the channel walls would be far more ideal. A possible (but challenging) approach that we are experimenting with is the incorporation of locally deformable 'diaphragm' sections in the channel walls by thinning of the same fused silica substrate material during the SLE fabrication. The pressure measurement would involve optical detection of the diaphragm displacement under flow.

However, the most obvious and probably fruitful future perspective for SLE lies in the opportunity to fabricate truly 3D flow geometries (e.g. channels with arbitrary shapes of cross-section, offset inlets/outlets and axisymmetric geometries, see Figure 6c and d and Ref. [38]), which promises a huge variety of new research directions for microscale fluid dynamical studies. Apart from fundamental studies, it is possible to conceive of extremely complex 3D geometries designed to model 'real' flows, for example, through intersecting blood vessels or around the bodies of microorganisms. This is also an extremely timely opportunity coinciding with the current emergence of sophisticated commercially available stereoscopic microparticle velocimetry

techniques, which enable microscale 3D flows to be studied in detail [66].

Conflict of interest statement

Nothing declared.

References

Papers of particular interest, published within the period of review, have been highlighted as:

   * of special interest
  ** of outstanding interest

1. McDonald JC, Whitesides GM: **Poly(dimethylsiloxane) as a**
 * **material for fabricating microfluidic devices**. *Accounts Chem Res* 2002, **35**:491–499, https://doi.org/10.1021/ar010110q.
Seminal article detailing the use of soft lithography for the fabrication of microfluidic devices.

2. Stone HA, Stroock AD, Ajdari A: **Engineering flows in small devices: microfluidics toward a lab-on-a-chip**. *Annu Rev Fluid Mech* 2004, **36**:381–411, https://doi.org/10.1146/annurev.fluid.36.050802.122124.

3. Squires TM, Quake SR: **Microfluidics: fluid physics at the**
** **nanoliter scale**. *Rev Mod Phys* 2005, **77**:977–1026, https://doi.org/10.1103/RevModPhys.77.977.
Review article that provides an excellent overview of fluid physics at the microscale.

4. Whitesides GM: **The origins and the future of microfluidics**. *Nature* 2006, **442**:368–373, https://doi.org/10.1038/nature05058.

5. Poole RJ: **The deborah and Weissenberg numbers**. *Rheology Bulletin* 2012, **53**:32–39.

6. Perkins TT, Smith DE, Chu S: **Single polymer dynamics in an elongational flow**. *Science* 1997, **276**:2016–2021, https://doi.org/10.1126/science.276.5321.2016.

7. Schroeder CM, Babcock HP, Shaqfeh ESG, Chu S: **Observation of polymer conformation hysteresis in extensional flow**. *Science* 2003, **301**:1515–1519, https://doi.org/10.1126/science.1086070.

8. Shaqfeh ESG: **The dynamics of single-molecule DNA in flow**. *J Non-Newtonian Fluid Mech* 2005, **130**:1–28, https://doi.org/10.1016/j.jnnfm.2005.05.011.

9. Stone PA, Hudson SD, Dalhaimer P, Discher DE, Amis EJ, Migler KB: **Dynamics of wormlike micelles in elongational flows**. *Macromolecules* 2006, **39**:7144–7148, https://doi.org/10.1021/ma0611016.

10. Lee JS, Shaqfeh ESG, Muller SJ: **Dynamics of DNA tumbling in shear to rotational mixed flows: pathways and periods**. *Phys Rev E* 2007, **75**:040802, https://doi.org/10.1103/PhysRevE.75.040802.

11. Gulati S, Muller SJ, Liepmann D: **Direct measurements of viscoelastic flows of DNA in a 2:1 abrupt planar microcontraction**. *J Non-Newtonian Fluid Mech* 2008, **155**:51–66, https://doi.org/10.1016/j.jnnfm.2008.05.005.

12. Groisman A, Steinberg V: **Efficient mixing at low Reynolds number using polymer additives**. *Nature* 2001, **410**:905–908, https://doi.org/10.1038/35073524.

13. Groisman A, Enzelberger M, Quake SR: **Microfluidic memory and control devices**. *Science* 2003, **300**:955−958, https://doi.org/10.1126/science.1083694.

14. Rodd LE, Scott TP, Boger DV, Cooper-White JJ, McKinley GH: **The inertio-elastic planar entry flow of low-viscosity elastic fluids in micro-fabricated geometries**. *J Non-Newtonian Fluid Mech* 2005, **129**:1−22, https://doi.org/10.1016/j.jnnfm.2005.04.006.

15. Arratia PE, Thomas CC, Diorio J, Gollub JP: **Elastic instabilities of polymer solutions in cross-channel flow**. *Phys Rev Lett* 2006, **96**:144502, https://doi.org/10.1103/PhysRevLett.96.144502.

16. Pathak JA, Hudson SD: **Rheo-optics of equilibrium polymer solutions: wormlike micelles in elongational flow in a microfluidic cross-slot**. *Macromolecules* 2006, **39**:8782−8792, https://doi.org/10.1021/ma061355r.

17. Phelan FR, Hughes NR, Pathak JA: **Chaotic mixing in microfluidic devices driven by oscillatory cross flow**. *Phys Fluids* 2008, **20**:023101, https://doi.org/10.1063/1.2830550.

18. Soulages J, Oliveira MSN, Sousa PC, Alves MA, McKinley GH: **Investigating the stability of viscoelastic stagnation flows in T-shaped microchannels**. *J Non-Newtonian Fluid Mech* 2009, **163**:9−24, https://doi.org/10.1016/j.jnnfm.2009.06.002.

19. Nghe P, Fielding SM, Tabeling P, Ajdari A: **Interfacially driven instability in the microchannel flow of a shear-banding fluid**. *Phys Rev Lett* 2010, **104**:248303, https://doi.org/10.1103/PhysRevLett.104.248303.

20. Haward SJ, McKinley GH: **Stagnation point flow of wormlike micellar solutions in a microfluidic cross-slot device: effects of surfactant concentration and ionic environment**. *Phys Rev E* 2012, **85**:031502−031514, https://doi.org/10.1103/PhysRevE.85.031502.

21. Haward SJ, Galindo-Rosales FJ, Ballesta P, Alves MA: **Spatio-temporal flow instabilities of wormlike micellar solutions in rectangular microchannels**. *Appl Phys Lett* 2014, **104**:124101, https://doi.org/10.1063/1.4869476.

22. Pan L, Morozov A, Wagner C, Arratia PE: **Non-linear elastic instability in channel flows at low Reynolds number**. *Phys Rev Lett* 2013, **110**:174502, https://doi.org/10.1103/PhysRevLett.110.174502.

23. Zilz J, Schäfer C, Wagner C, Poole RJ, Alves MA, Lindner A: **Serpentine channels: micro-rheometers for fluid relaxation times**. *Lab Chip* 2014, **14**:351−358, https://doi.org/10.1039/c3lc50809a.

24. Sousa PC, Pinho FT, Oliveira MSN, Alves MA: **Purely elastic flow instabilities in microscale cross-slot devices**. *Soft Matter* 2015, **11**:8856−8862, https://doi.org/10.1039/c5sm01298h.

25. Shi X, Christopher GF: **Growth of viscoelastic instabilities around linear cylinder arrays**. *Phys Fluids* 2016, **28**:124102, https://doi.org/10.1063/1.4968221.

26. Qin B, Arratia PE: **Characterizing elastic turbulence in channel flows at low Reynolds number**. *Phys Rev Fluids* 2017, **2**:083302, https://doi.org/10.1103/PhysRevFluids.2.083302.

27. Sousa PC, Pinho FT, Alves MA: **Purely elastic flow instabilities and elastic turbulence in microfluidic cross-slot devices**. *Soft Matter* 2018, **14**:1344−1354, https://doi.org/10.1039/c7sm01106g.

28. Gardner K, Pike ER, Miles MJ, Keller A, Tanaka K: **Photon-correlation velocimetry of polystyrene solutions in extensional flow-fields**. *Polymer* 1982, **23**:1435−1442, https://doi.org/10.1016/0032-3861(82)90240-3.
*
An example of a very early use of microfluidics in a non-Newtonian flow context, employing a hand-made "cross-slot" device to study the extensional flow of dilute polymer solutions. Elastic flow instabilities were reported that were only much later studied in detail and which are of great current interest.

29. Odell JA, Keller A: **Flow-induced chain fracture of isolated linear macromolecules in solution**. *J Polym Sci, Part B: Polym Phys* 1986, **24**:1889−1916, https://doi.org/10.1002/polb.1986.090240901.

30. Fuller GG: *Optical rheometry of complex fluids*. New York: Oxford University Press; 1995.

31. Doutel E, Carneiro J, Oliveira MSN, Campos JBLM, Miranda JM: **Fabrication of 3D mili-scale channels for hemodynamic studies**. *J Mech Med Biol* 2015, **15**:1550004, https://doi.org/10.1142/S0219519415500049.

32. Kang K, Oh S, Yi H, Han S, Hwang Y: **Fabrication of truly 3D microfluidic channel using 3d-printed soluble mold**. *Biomicrofluidics* 2018, **12**:014105, https://doi.org/10.1063/1.5012548.

33. Thompson BL, Ouyang Y, Duarte GRM, Carrilho E, Krauss ST, Landers JP: **Inexpensive, rapid prototyping of microfluidic devices using overhead transparencies and a laser print, cut and laminate fabrication method**. *Nat Protoc* 2015, **10**:866−875, https://doi.org/10.1038/nprot.2015.051.

34. Haward SJ, Sharma V, Odell JA: **Extensional opto-rheometry with biofluids and ultra-dilute polymer solutions**. *Soft Matter* 2011, **7**:9908−9921, https://doi.org/10.1039/c1sm05493g.

35. Guckenberger DJ, de Groot TE, Wan AMD, Beebe DJ, Young EWK: **Micromilling: a method for ultra-rapid prototyping of plastic microfluidic device**. *Lab Chip* 2015, **15**:2364−2378, https://doi.org/10.1039/c5lc00234f.

36. Iliescu C, Taylor H, Avram M, Miao J, Franssila S: **A practical guide for the fabrication of microfluidic devices using glass and silicon**. *Biomicrofluidics* 2012, **6**:016505, https://doi.org/10.1063/1.3689939.

37. Gottmann J, Hermans M, Ortmann J: **Digital photonic produc-
* tion of micro structures in glass by in-volume selective laser-induced etching using a high speed micro scanner**. *Physics Procedia* 2012, **39**:534−541, https://doi.org/10.1016/j.phpro.2012.10.070.
Provides a detailed description of the selective laser-induced etching fabrication process.

38. Meineke G, Hermans M, Klos J, Lenenbach A, Noll R:
* **A microfluidic opto-caloric switch for sorting of particles by using 3D-hydrodynamic focusing based on SLE fabrication capabilities**. *Lab Chip* 2016, **16**:820−828, https://doi.org/10.1039/C5LC01478F.
Demonstrates the use of selective laser-induced etching for the fabrication of complex three-dimensional microfluidic channels in fused silica glass, with a specific application to particle sorting.

39. Zhao Y, Shen AQ, Haward SJ: **Flow of wormlike micellar solutions around confined microfluidic cylinders**. *Soft Matter* 2016, **12**:8666−8681, https://doi.org/10.1039/c6sm01597b.

40. Haward SJ, Toda-Peters K, Shen AQ: **Steady viscoelastic flow
** around high-aspect-ratio, low-blockage-ratio microfluidic cylinders**. *J Non-Newtonian Fluid Mech* 2018, **254**:23−35, https://doi.org/10.1016/j.jnnfm.2018.02.009.
Article featuring the use of selective laser-induced etching to fabricate high aspect ratio microchannels containing extremely slender circular posts. This demonstrates the potential of SLE to push microfluidics into new geometrical regimes.

41. Wereley ST, Meinhart CD: **Recent advances in micro-particle image velocimetry**. *Annu Rev Fluid Mech* 2010, **42**:557−576, https://doi.org/10.1146/annurev-fluid-121108-145427.

42. Zenit R, Feng JJ: **Hydrodynamic interactions among bubbles, drops, and particles in non-Newtonian liquids**. *Annu Rev Fluid Mech* 2018, **50**:505−534, https://doi.org/10.1146/annurev-fluid-122316-045114.

43. Haward SJ: **Microfluidic extensional rheometry using stagnation point flow**. *Biomicrofluidics* 2016, **10**:043401, https://doi.org/10.1063/1.4945604.

44. Kerr OS, Dold JW: **Periodic steady vortices in a stagnation-point flow**. *J Fluid Mech* 1994, **276**:307−325, https://doi.org/10.1017/S0022112094002570.

45. Burgers JM: **A mathematical model illustrating the theory of turbulence**. *Adv Appl Mech* 1948, **1**:171−199, https://doi.org/10.1016/S0065-2156(08)70100-5.

46. Haward SJ, Poole RJ, Alves MA, Oliveira PJ, Goldenfeld N, Shen AQ: **Tricritical spiral vortex instability in cross-slot flow**. *Phys Rev E* 2016, **93**:031101, https://doi.org/10.1103/PhysRevE.93.031101.

47. Ait Mouheb N, Montillet A, Solliec C, Havlica J, Legentilhomme P, Comiti J, Tihon J: **Flow characterization in T-shaped and cross-shaped micromixers**. *Microfluid Nanofluidics* 2011, **10**: 1185–1197, https://doi.org/10.1007/s10404-010-0746-5.

48. Burshtein N, Zografos K, Shen AQ, Poole RJ, Haward SJ:
** **Inertioelastic flow instability at a stagnation point**. *Phys Rev X* 2017, **7**:041039, https://doi.org/10.1103/PhysRevX.7.041039.
Our first use of selective laser-induced etching for the fabrication of microdevices for visualizing 3D flows – here applied to observe the effects of dilute polymer additives on the formation of streamwise stretched vortices.

49. Zografos K, Burshtein N, Shen AQ, Haward SJ, Poole RJ: **Elastic modifications of an inertial instability in a 3D cross-slot**. *J Non-Newtonian Fluid Mech* 2018, **262**:12–24, https://doi.org/10.1016/j.jnnfm.2018.02.002.

50. Virk PS, Baher H: **The effect of polymer concentration on drag reduction**. *Chem Eng Sci* 1970, **25**:1183–1189, https://doi.org/10.1016/0009-2509(70)85008-4.

51. White CM, Mungal MG: **Mechanics and prediction of turbulent drag reduction with polymer additives**. *Annu Rev Fluid Mech* 2008, **40**:235–256, https://doi.org/10.1146/annurev.fluid.40.111406.102156.

52. Chen KK, Rowley CW, Stone HA: **Vortex dynamics in a pipe T-junction: recirculation and sensitivity**. *Phys Fluids* 2015, **27**: 034107, https://doi.org/10.1063/1.4916343.

53. Oettinger D, Ault JT, Stone HA, Haller G: **Invisible anchors trap particles in branching junctions**. *Phys Rev Lett* 2018, **121**: 054502, https://doi.org/10.1103/PhysRevLett.121.054502.

54. Poole RJ, Alves MA, Oliveira PJ: **Purely elastic flow asymmetries**. *Phys Rev Lett* 2007, **99**:164503, https://doi.org/10.1103/PhysRevLett.99.164503.

55. Vigolo D, Radl S, Stone HA: **Unexpected trapping of particles at a T-junction**. *Proc Natl Acad Sci Unit States Am* 2014, **111**: 4770–4775, https://doi.org/10.1073/pnas.1321585111.

56. Ault JT, Fani A, Chen KK, Shin S, Gallaire F, Stone HA: **Vortex-breakdown-induced particle capture in branching junctions**. *Phys Rev Lett* 2016, **117**:084501, https://doi.org/10.1103/PhysRevLett.117.084501.

57. Chan ST, Haward SJ, Shen AQ: **Microscopic investigation of
** **vortex breakdown in a dividing T-junction flow**. *Phys Rev Fluids* 2018, **3**:072201, https://doi.org/10.1103/PhysRevFluids.3.072201.
This article details the use of selective laser-induced etching to fabricate T-shaped microchannels. New insights are presented into the phenomenon of vortex breakdown in inertial microfluidics.

58. Charru F, Hinch EJ: **'Phase diagram' of interfacial instabilities in a two-layer Couette flow and mechanism of the long-wave instability**. *J Fluid Mech* 2000, **414**:195–223, https://doi.org/10.1017/S002211200000851X.

59. Page J, Zaki TA: **Viscoelastic shear flow over a wavy surface**. *J Fluid Mech* 2016, **801**:392–429, https://doi.org/10.1017/jfm.2016.455.

60. Haward SJ, Shen AQ, Page J, Zaki TA: **Poiseuille flow over a
** **wavy surface**. *Phys Rev Fluids* 2017, **2**:124102, https://doi.org/10.1103/PhysRevFluids.2.124102.
In this article, selective laser-induced etching is employed to fabricate high aspect ratio microchannels featuring small amplitude sinusoidal wavy surfaces. Flow patterns in the microchannels are shown to match the predictions of linear theory, both exemplifying the accuracy and precision of the fabrication and providing an experimental confirmation of the theory for the first time.

61. Haward SJ, Page J, Zaki TA, Shen AQ: **Inertioelastic Poiseuille flow over a wavy surface**. *Phys Rev Fluids* 2018, **3**:091302, https://doi.org/10.1103/PhysRevFluids.3.091302.

62. Haward SJ, Page J, Zaki TA, Shen AQ: **"Phase diagram" for viscoelastic Poiseuille flow over a wavy surface**. *Phys Fluids* 2018, **30**:011811, https://doi.org/10.1063/1.5057392.

63. Samanta D, Dubief Y, Holzner M, Scäfer C, Morozov AN, Wagner C, Hof B: **Elasto-inertial turbulence**. *Proc Natl Acad Sci USA* 2013, **110**:10557–10562, https://doi.org/10.1073/pnas.1219666110.

64. Dey AA, Modarres-Sadeghi Y, Rothstein JP: **Experimental
** **observation of viscoelastic fluid-structure interactions**. *J Fluid Mech* 2017, **813**:R5, https://doi.org/10.1017/jfm.2017.15.
A seminal study of the interactions between a viscoelastic flow instability and a deformable structure in the flow. The 3D microfabrication capacity of SLE has a great potential to make an impact in this emergent field.

65. Dey AA, Modarres-Sadeghi Y, Rothstein JP: **Viscoelastic fluid-structure interactions between a flexible cylinder and worm-like micellar solution**. *Phys Rev Fluids* 2018, **3**:063301, https://doi.org/10.1103/PhysRevFluids.3.063301.

66. Lindken R, Westerweel J, Wieneke B: **Stereoscopic micro particle image velocimetry**. *Exp Fluid* 2006, **41**:161–171, https://doi.org/10.1007/s00348-006-0154-5.